

# Revisiting the Physical Mechanisms of East Asian Summer Monsoon Precipitation Changes During the Mid-Holocene: A Data–model Comparison

Yong Sun (✉ [sunyong@mail.iap.ac.cn](mailto:sunyong@mail.iap.ac.cn))

Institute of Atmospheric Physics Chinese Academy of Sciences <https://orcid.org/0000-0002-1087-6060>

Haibin Wu

IGG CAS: Institute of Geology and Geophysics Chinese Academy of Sciences

Gilles Ramstein

LSCE: Laboratoire des sciences du climat et de l'environnement

Bo Liu

CUG: China University of Geosciences

Yan Zhao

ITPCAS: Institute of Tibetan Plateau Research Chinese Academy of Sciences

Laurent Li

LMD: Laboratoire de Meteorologie Dynamique

Xiayu Yuan

IAP CAS: Institute of Atmospheric Physics Chinese Academy of Sciences

Wenchao Zhang

IGG CAS: Institute of Geology and Geophysics Chinese Academy of Sciences

Lijuan Li

IAP CAS: Institute of Atmospheric Physics Chinese Academy of Sciences

Liwei Zou

IAP CAS: Institute of Atmospheric Physics Chinese Academy of Sciences

Tianjun Zhou

IAP CAS: Institute of Atmospheric Physics Chinese Academy of Sciences

---

## Research Article

**Keywords:** Mid-Holocene, Monsoon precipitation, Water vapor budget, Thermodynamic effect, Dynamic effect, Cloud cooling effect

**Posted Date:** April 20th, 2021

**DOI:** <https://doi.org/10.21203/rs.3.rs-390166/v1>

**License:**  This work is licensed under a Creative Commons Attribution 4.0 International License.

[Read Full License](#)

---

1 **Revisiting the physical mechanisms of East Asian Summer Monsoon**  
2 **precipitation changes during the mid-Holocene: A data–model**  
3 **comparison**

4 **Yong Sun<sup>1,2</sup>, Haibin Wu<sup>3,4,5</sup>, Gilles Ramstein<sup>2</sup>, Bo Liu<sup>6</sup>, Yan Zhao<sup>7</sup>, Laurent Li<sup>8</sup>, Xiayu**  
5 **Yuan<sup>9</sup>, Wenchao Zhang<sup>3</sup>, Lijuan Li<sup>1</sup>, Liwei Zou<sup>1</sup>, Tianjun Zhou<sup>1,10</sup>**

6

7 <sup>1</sup>State Key Laboratory of Numerical Modeling for Atmospheric Sciences and Geophysical  
8 Fluid Dynamics, Institute of Atmospheric Physics, Chinese Academy of Sciences, Beijing  
9 100029, China

10 <sup>2</sup>Laboratoire des Sciences du Climat et de l'Environnement, LSCE/IPSL, CEA - CNRS -  
11 UVSQ, Université Paris - Saclay, Gif - sur - Yvette, France

12 <sup>3</sup>Key Laboratory of Cenozoic Geology and Environment, Institute of Geology and  
13 Geophysics, Chinese Academy of Sciences, Beijing 100029, China

14 <sup>4</sup>CAS Center for Excellence in Life and Paleoenvironment, Beijing, 100044, China

15 <sup>5</sup>University of Chinese Academy of Sciences, Beijing, 100049, China

16 <sup>6</sup>Department of Atmospheric Science, School of Environmental Studies, China University  
17 of Geoscience, Wuhan 430074, China

18 <sup>7</sup>Institute of Tibetan Plateau research, Chinese Academy of Sciences, Beijing, 100101,  
19 China

20 <sup>8</sup>Laboratoire de Météorologie Dynamique, CNRS, Sorbonne Université, Ecole Normale

21 Supérieure, Ecole Polytechnique, Paris, France

22 <sup>9</sup>Editorial Office of Advances in Atmospheric Sciences, Institute of Atmospheric Physics,  
23 Chinese Academy of Sciences, Beijing 100029, China

24 <sup>10</sup>CAS Center for Excellence in Tibetan Plateau Earth Sciences, Chinese Academy of  
25 Sciences (CAS), Beijing, 100101, China

26 Corresponding author: Yong Sun (sunyong@mail.iap.ac.cn)

27 **Key points:**

- 28 ● Quantitative data–model comparison shows an overall increase except for local  
29 decrease in EASM precipitation during the MH.
- 30 ● Dynamic enhancement of horizontal moisture advection increases EASM precipitation  
31 in both proxy records and simulations.
- 32 ● The thermodynamic increase of horizontal moisture advection in precipitation in both  
33 the proxy records and simulations is reduced by a cloud cooling effect.
- 34 ● Decreasing precipitation in both the proxy records and models can be largely explained  
35 by the coupled thermodynamic and dynamic effects on horizontal moisture advection

36 **Abstract**

37 The mid-Holocene (MH; 6 ka) is one of the benchmark periods for the Paleoclimate  
38 Modeling Intercomparison Project (PMIP) and provides a unique opportunity to study  
39 monsoon dynamics and orbital forcing (i.e., mostly precession) that differ significantly  
40 from the present day. We conducted a data–model comparison along with a dynamic  
41 analysis to investigate monsoonal (i.e., East Asian summer monsoon; EASM) precipitation  
42 changes over East Asia during the MH. We used the three phases of the PMIP simulations  
43 for the MH, and quantitatively compared the model results with pollen-based climate  
44 records. The data–model comparison shows an overall increase in precipitation, except for  
45 a local decrease in EASM precipitation during the MH. Decomposition of the moisture  
46 budget into thermodynamic, dynamic components and co-variations in both allowed us to  
47 assess the relative role of thermodynamic and dynamic components in controlling EASM  
48 precipitation during the MH, and to investigate the precipitation changes obtained from  
49 pollen records in terms of physical processes. We show that the dynamic effect, rather than  
50 the thermodynamic effect, is the dominant control in increased EASM precipitation during  
51 the MH in both the proxy records and models. The dynamic increase in precipitation results  
52 mainly from the enhancement of horizontal monsoonal moisture transport that is caused by  
53 intensified stationary eddy horizontal circulation over East Asia. In addition, a cloud  
54 cooling effect reduced the thermodynamic contribution to the increase in EASM  
55 precipitation during the MH.

56 **Keywords:** Mid-Holocene, Monsoon precipitation, Water vapor budget, Thermodynamic  
57 effect, Dynamic effect, Cloud cooling effect

58

59 **1. Introduction**

60 The mid-Holocene (MH; *ca.* 6 ka) is part of the current interglacial period. This period was  
61 characterized by a large change in precession, which led to an enhanced seasonal cycle,  
62 whereas greenhouse gases (GHGs) were similar to pre-industrial (PI) levels and continental  
63 configurations were almost identical to the present day. Therefore, the MH is an ideal  
64 period for studying the orbital-forcing of Earth’s climate (Steig 1999; Shin et al. 2006).

65 Paleoclimatic reconstructions and simulations based on the Paleoclimate Modeling  
66 Intercomparison Project (PMIP) protocols are important approaches for investigating  
67 large-scale MH climate features and the mechanisms driving climate changes. In general,  
68 data–model comparisons have shown similar annual mean monsoonal precipitation  
69 changes during the MH compared with the PI period (COHMAP Members 1988;  
70 Braconnot et al. 2012; Zhao and Harrison 2012; Jiang et al. 2015; Jiang et al. 2019; Lin et  
71 al. 2019; D’Agostino et al. 2019, 2020). Solar radiation increases (decreases) in the boreal  
72 (austral) summer acted as the main driver of strengthening (weakening) of the Northern  
73 (Southern) Hemisphere monsoon in the MH (Joussaume et al. 1999; Zhao and Harrison  
74 2012; Jiang et al. 2015; Brierley et al. 2020). In addition to the direct response to solar  
75 forcing, regional monsoonal precipitation changes are also influenced by feedback from  
76 vegetation expansion, dust reduction (Patricola and Cook 2007; Pausata et al. 2016;  
77 Hopcroft and Valdes 2019; Piao et al. 2020), and oceanic processes (Liu et al. 2004; Zhao  
78 et al. 2005; Zhao and Harrison 2012). The “Green Sahara” involved the northward  
79 extension of vegetation in North Africa during the MH, which increased Northern  
80 Hemisphere on-land monsoonal precipitation (Sun et al. 2019) and shifted the East Asian  
81 summer monsoon (EASM) northward (Piao et al. 2020). The vegetated Sahara induced

82 changes in Walker and Hadley circulations, enhanced the western Pacific subtropical high  
83 (WPSH), and strengthened the EASM (Piao et al. 2020).

84 An increasing number of studies have used dynamic diagnostics to improve our  
85 understanding of regional rainfall processes during the MH. Using a moisture budget  
86 analysis, D'Agostino et al. (2019) examined the impact of thermodynamic and dynamic  
87 components on the Northern Hemisphere monsoon response to MH orbital forcing, and  
88 found that dynamic processes were the dominant contributor to increased monsoon  
89 precipitation in the MH. This increase in precipitation due to the dynamic effect can largely  
90 be explained by enhanced vertical motion due to local diabatic heating of the atmospheric  
91 column (D'Agostino et al. 2019). Although D'Agostino et al. (2019) did not consider the  
92 EASM due to the hybrid nature of the tropical and subtropical monsoon with impacts from  
93 mid and high-latitudes (Ding and Chan 2005), the findings were found to be valid for the  
94 EASM by Wang et al. (2020). However, it remains unclear why the thermodynamic  
95 contribution to monsoon precipitation changes during the MH was weak. In addition to the  
96 key role of vertical moisture advection (Wang et al. 2020), it remains to be determined  
97 whether a dynamic increase in MH precipitation can be achieved through enhancement of  
98 horizontal monsoon circulation. In addition, the simulated EASM precipitation changes  
99 during the MH have not been validated by proxy records. Therefore, the response of the  
100 EASM climate to orbital forcing during the MH is not fully understood.

101 In this study, we first conducted a quantitative data–model comparison of EASM  
102 precipitation changes during the MH. We then reconciled the data–model comparison by  
103 comparing decomposed physical processes that affect the moisture budget.

104

105 **2 Materials and methods**

106 **2.1 Three phases of PMIP simulations for MH climate**

107 MH simulations using the three phases of PMIP (PMIP2, PMIP3, and PMIP4) were used  
108 to provide a dynamic understanding of EASM precipitation variations at orbital timescales.  
109 The same orbital parameter configurations (eccentricity = 0.018682; obliquity = 24.105°;  
110 angular precession = 0.87°) were used in all three PMIP phases for the MH, but in the PI  
111 runs slight differences in the reference periods were chosen for the three PMIP phases  
112 (Braconnot et al. 2007, 2012; Otto-Bliesner et al. 2017). Orbital forcing of the PI runs in  
113 PMIP2 and PMIP3 was set to 1950, and the orbital parameters in 1850 were applied to the  
114 PI run in PMIP4.

115 In addition, there are two differences in GHG concentrations for PMIP4 compared with  
116 PMIP2 and PMIP3: (1) the same trace gas concentrations ( $\text{CO}_2 = 280$  ppm;  $\text{N}_2\text{O} = 270$  ppb)  
117 were used for the MH and PI periods under the PMIP2 and PMIP3 protocols, except for a  
118 reduction in  $\text{CH}_4$  (from 760 ppb in the PI period to 650 ppb in the MH); (2) PMIP4 utilized  
119 different GHG concentrations for the PI period ( $\text{CO}_2 = 284.3$  ppm;  $\text{CH}_4 = 808.2$  ppb;  $\text{N}_2\text{O}$   
120 = 273.0 ppb) and MH ( $\text{CO}_2 = 264.4$  ppm;  $\text{CH}_4 = 597$  ppb;  $\text{N}_2\text{O} = 262.0$  ppb) simulations.  
121 In addition, the solar constant used by PMIP4 (1360.7  $\text{W}/\text{m}^2$ ) is lower than that used in  
122 PMIP2 and PMIP3 (1365  $\text{W}/\text{m}^2$ ). More details of the PMIP models used for the MH  
123 simulations are presented in Tables S1 and S2. In brief, the climate change during the MH  
124 obtained from PMIP simulations is broadly consistent with theory and observations,  
125 including increased summer warming of the Northern Hemisphere and associated shifts in  
126 tropical rainfall. Biases in the magnitude and sign of regional responses are similar in

127 PMIP2, PMIP3, and PMIP4, despite the improvement of the models in complexity and  
128 resolution (Braconnot et al. 2012; Brierley et al. 2020).

129 In this study, we generally present findings based on the multi-model ensembles (MMEs)  
130 mean of PMIP3 and PMIP4, except for Fig. 1, which shows results from the MMEs of all  
131 three PMIP phases, because all three phases of PMIP yield similar surface climate  
132 simulations for East Asia during the MH. The individual MME results for each PMIP phase  
133 are given in the online Supplementary Materials.

134

## 135 **2.2 Methodology**

### 136 **2.2.1 Moisture budget**

137 The water vapor budget equation was used to constrain the physical processes that control  
138 the monsoonal precipitation variations on orbital timescales. The time-mean column-  
139 integrated moisture budget can be expressed as:

$$140 \quad P = E - \langle \omega \partial_p q \rangle - \langle \vec{V}_H \cdot \nabla q \rangle + Res \quad (1)$$

141 where  $P$  is the precipitation,  $E$  is the evaporation,  $\omega$  is the vertical velocity at a constant  
142 pressure coordinate,  $q$  is the atmospheric specific humidity,  $V_H$  is the horizontal wind  
143 velocity, and  $Res$  is a residual term including transient eddy influences and their potential  
144 role in shaping EASM precipitation that was not addressed due to the unavailability of  
145 daily output from most PMIP models. By designating the column mass integrals with angle  
146 brackets,  $\langle \cdot \rangle = \int_0^{p_s} \cdot dp/g$ , where  $P_s$  is the surface pressure (Chou and Lan 2012). The  
147 difference in each term in Eq. 1 between the MH and PI period can be written as follows:

$$148 \quad \delta P = \delta E - \delta \langle \omega \partial_p q \rangle - \delta \langle \vec{V}_H \cdot \nabla q \rangle + \delta Res \quad (2)$$

149 To assess the relative importance of moisture content and atmospheric circulation changes

150 on moisture transport, variations in two advection terms were further decomposed into  
 151 linear contributions from the thermodynamic component (TC) and dynamic component  
 152 (DC), and non-linear contribution from the quadratic term (NL). TC was calculated as an  
 153 advective variation caused by changes in specific humidity with a fixed atmospheric  
 154 circulation, and DC is represented by changes in atmospheric circulation at a constant  
 155 specific humidity. NL was obtained from simultaneous changes in both atmospheric  
 156 circulation and specific humidity (Seager et al. 2010). The relationships between TC, DC,  
 157 and NL and changes in  $-\langle \vec{V}_H \cdot \nabla q \rangle$  can be expressed as:

$$158 \quad \text{TC} = -\langle \overline{\vec{V}_H} \cdot \nabla \delta q \rangle = -\int_0^{P_s} \overline{\vec{V}_H} \cdot \nabla \delta q \, dp \quad (3)$$

$$159 \quad \text{DC} = -\langle \delta \vec{V}_H \cdot \nabla \bar{q} \rangle = -\int_0^{P_s} \delta \vec{V}_H \cdot \nabla \bar{q} \, dp \quad (4)$$

$$160 \quad \text{NL} = -\langle \delta \vec{V}_H \cdot \nabla \delta q \rangle = -\int_0^{P_s} \delta \vec{V}_H \cdot \nabla \delta q \, dp \quad (5)$$

161 Similarly, the decomposition of changes in  $-\langle \omega \partial_p q \rangle$  into TC, DC, and NL can be written  
 162 as:

$$163 \quad \text{TC} = -\langle \overline{\omega} \partial_p \delta q \rangle = -\int_0^{P_s} \overline{\omega} \partial_p \delta q \, dp \quad (6)$$

$$164 \quad \text{DC} = -\langle \delta \omega \partial_p \bar{q} \rangle = -\int_0^{P_s} \delta \omega \partial_p \bar{q} \, dp \quad (7)$$

$$165 \quad \text{NL} = -\langle \delta \omega \partial_p \delta q \rangle = -\int_0^{P_s} \delta \omega \partial_p \delta q \, dp \quad (8)$$

166

### 167 **2.2.2 Climate feedback response analysis method**

168 The climate feedback response analysis method (CFRAM) was used to quantify the relative  
 169 contributions of nine separate processes on surface temperature differences between the  
 170 MH and PI period. The CFRAM formula is (Cai and Lu 2009; Lu and Cai 2009):

$$\begin{aligned}
171 \quad \Delta T_{\text{MH-PI}} &= \left( \frac{\partial \mathbf{R}}{\partial \mathbf{T}} \right)^{-1} (\Delta \mathbf{S}^{\text{SI}} + \Delta \mathbf{S}^{\alpha} + \Delta(\mathbf{S} - \mathbf{R})^{\text{wv}} + \Delta(\mathbf{S} - \mathbf{R})^{\text{cld}} + \Delta(\mathbf{S} - \mathbf{R})^{\text{CH}_4} + \Delta \mathbf{Q}^{\text{SH}} + \Delta \mathbf{Q}^{\text{LH}} \\
172 \quad &+ \Delta \mathbf{Q}^{\text{AHT}} + \Delta \mathbf{Q}^{\text{Surface\_dynamics}}) \quad (9)
\end{aligned}$$

173 where  $\left( \frac{\partial \mathbf{R}}{\partial \mathbf{T}} \right)$  is the Planck feedback matrix and the superscripts SI,  $\alpha$ , wv, cld, and CH<sub>4</sub>  
174 denote the surface temperature changes induced by solar insolation, surface albedo, water  
175 vapor, cloud, and methane, respectively. The superscripts SH, LH, AHT, and  
176 Surface\_dynamics are the surface temperature changes due to sensible heat, latent heat,  
177 atmospheric heat transport, and surface dynamics. The advantage of this method is that it  
178 allows the actual processes that are responsible for the reduced thermodynamic increase in  
179 monsoonal precipitation to be distinguished (Fig. 2c and Figure 6e).

180

### 181 **2.2.3 EASM domains**

182 The EASM domains of this study follow the definition of Wang et al. (2012). The two  
183 required conditions are: (1) the annual range of precipitation rates (defined as local summer  
184 minus local winter) is >2 mm/day; (2) the local summer precipitation is >55% of total  
185 annual rainfall. The local summer includes May–June–July–August–September and local  
186 winter includes November–December–January–February–March. Given the inter-model  
187 spread of EASM domains across the MH and PI simulations, and slight differences in the  
188 EASM domains between the MH and PI periods, the results were averaged over the EASM  
189 domain of each model.

## 190 **3. Results**

### 191 **3.1 Quantitative data–model comparison over the EASM domain**

192 Figure 1 shows the surface air temperature (SAT) and precipitation (PRECIP) changes  
193 during the MH compared with the PI period. SAT changes during the MH are non-uniform  
194 across the EASM domain (Fig. 1a). This is reflected by southern cooling (south of 30°N)  
195 and northern warming (north of 30°N; Fig. 1a). Consequently, these variations in SAT  
196 changes are associated with a reduction in meridional thermal contrast over the monsoonal  
197 domain, and its potential effects on the MH monsoonal precipitation are addressed in  
198 section 3.3.1.

199 There is an overall increase in EASM precipitation during the MH, except for a decrease  
200 in a few parts of the monsoon area in both the proxy data and simulations (Figs 1b-c and  
201 S1). Out of 147 pollen-based reconstruction sites, 126 show an EASM precipitation  
202 increase under the warm MH conditions (Fig. 1b), and the remaining 21 sites show a  
203 precipitation decrease (Fig. 1b). The PMIP models generate wetter (drier) MH than PI  
204 conditions over most (few) parts of the EASM domain (Figs 1c and S1). However, there  
205 are distinct regions where the precipitation decreases during the MH (Figs 1b-c and S1),  
206 which are mostly in northern China. Decreases in the modeled precipitation are confined  
207 to regions of the eastern Tibetan Plateau.

208 We now use dynamic diagnostics to further examine the underlying cause of the spatial  
209 inhomogeneity in simulated precipitation, and thus reconcile the data–model comparison.

210

### 211 **3.2 Reconciling the data–model comparison by decomposition of the water vapor** 212 **budget**

213 **3.2.1 Decomposing the physical processes involved in the simulated precipitation**  
214 **changes**

215 An area-averaged moisture budget analysis was first undertaken over the EASM domain  
216 for the PI and MH periods (Fig. 2a). Evaporation and vertical moisture advection were  
217 identified as being the dominant contributors to the mean summer precipitation over East  
218 Asia in the PI and MH periods, whereas the horizontal moisture advection and residual  
219 terms were less important. There are large inter-model variations for each moisture budget  
220 term (Figs 2b and S2a). To reveal the potential mechanisms for this range, and quantify the  
221 relative roles of horizontal and vertical moisture transport in controlling precipitation  
222 changes, further decomposition of the two moisture advection terms was carried out (Figs  
223 2c and S2b). Despite the inter-model variations in each advection term, the signs of each  
224 term are largely consistent for all models (Figs 2c and S2b). For example, the three  
225 decomposed terms for total moisture advection (i.e., the sum of horizontal and vertical  
226 moisture advection) have a positive DC value, negative NL value, and negligible TC value  
227 compared with DC and NL. A positive DC value increases precipitation and a negative NL  
228 value leads to a precipitation decrease. There are distinct values for each decomposed  
229 process for the horizontal and vertical moisture advection (Fig. 2c). DC (NL) has an  
230 overwhelming effect on the precipitation increase (decrease), which is due mainly to  
231 strengthening (weakening) of the horizontal moisture advection. However, a much weaker  
232 precipitation increase is caused by the TC of the horizontal moisture advection. In summary,  
233 the horizontal moisture advection has a dominant role in the total moisture advection.

234

235 **3.2.2 Decoding the physical representation of pollen-based precipitation records**

236 Decomposition of the two moisture advection types was used to understand the physical  
237 processes involved in pollen-based precipitation records. Figure 3 shows a quantitative  
238 comparison of the pollen-based precipitation record with the three decomposed processes  
239 from the two moisture advection types (Fig. 3). The increase in precipitation from the proxy  
240 records are due mainly to intensified horizontal moisture advection (Fig. 3b). For example,  
241 106 of 126 proxy records show a precipitation increase that can be explained by dynamic  
242 enhancement of horizontal moisture advection (Fig. 3b). The remaining 20 proxy records  
243 show a precipitation increase that can be attributed to a weak increase in the TC of  
244 horizontal moisture advection (Fig. 3e). This is in good agreement with the limited role of  
245 the TC in increasing precipitation (Fig. 2c). In contrast, a decrease in precipitation in 21  
246 proxy records can be explained by the weakened NL of the horizontal moisture advection  
247 (Fig. 3h). In general, these results further support our previous modeling, in that horizontal  
248 moisture advection is the dominant control on the EASM precipitation changes during the  
249 MH.

250

### 251 **3.3 Physics of the moisture budget decomposition**

252 The moisture budget decomposition provides new insights into the data–model comparison.  
253 However, it is unclear what causes the dynamic enhancement of horizontal moisture  
254 advection and why the thermodynamic contribution to the precipitation increase is reduced  
255 during the MH. In addition, it is unknown whether the water vapor source of this dynamic  
256 enhancement has the same pathway as the EASM precipitation. Therefore, the physics  
257 underlying the thermodynamic and dynamic processes of horizontal moisture advection  
258 are further addressed in this section.

259

### 260 **3.3.1 Mechanisms of dynamic control on the precipitation**

261 The EASM domain and surrounding regions are dominated by stationary eddy horizontal  
262 circulation anomalies, as manifested by an anomalous cyclone confined to south of 30°N  
263 and a strong anticyclone to the north (Figs S3 and 4a–b). The regional horizontal moisture  
264 advection is enhanced by the cyclonic control over the EASM domain, and thus leads to a  
265 dynamic increase in EASM precipitation during the MH (Fig. 4b). Prominent easterly  
266 anomalies are observed between the cyclone and anticyclone (30°–45°N). This westerly  
267 weakening (i.e., easterly anomalies) can be explained by the thermal wind balance and the  
268 reduced meridional thermal contrast (Fig. 1a). In fact, the stationary eddy cyclone and  
269 anticyclone that contribute to regional enhancement of horizontal moisture advection over  
270 the EASM domain are a key part of the global-scale stationary wave trains, which emanate  
271 from anticyclones at Northern Hemisphere mid-latitudes to anticyclones at Southern  
272 Hemisphere mid-latitudes (Fig. 4a).

273 In contrast to the dynamic enhancement of horizontal moisture advection, the dynamic  
274 decrease of vertical moisture advection resulted in a drier eastern Tibetan Plateau during  
275 the MH (Figs 1c, S1, and 3c). This DC decreased the precipitation over the eastern Tibetan  
276 Plateau due to the stationary eddy vertical motion in this region. Ascending motion  
277 characterizes the western Tibetan Plateau and a descending motion occurs in the eastern  
278 Tibetan Plateau (Fig. 4b). In addition to a regional decrease in precipitation, the increase  
279 in the stationary eddy vertical motion also intensified the large-scale anti-Hadley  
280 circulation that consists of the ascending motion along the Himalaya and the descending  
281 motion coinciding with the ascending branch of the Hadley cell (i.e., ITCZ position; Fig.

282 4b). As a result, this intensified anti-Hadley circulation resulted in a large-scale decrease  
283 in precipitation in the tropics ( $0^{\circ}$ – $20^{\circ}$ N,  $60^{\circ}$ – $150^{\circ}$ E; Fig. S1).

284

### 285 **3.3.2 Water vapor source during dynamic enhancement of the precipitation**

286 Regional precipitation requires water vapor transport from remote source areas to the  
287 regions of precipitation. In mean JJA conditions, cross-equatorial airflow originates in the  
288 southern Indian Ocean, which is the main source of water vapor for EASM precipitation  
289 (Figs 5a and S4). It is important to consider the sources of water vapor for the dynamic  
290 enhancement of EASM precipitation during the MH. There are two major water vapor  
291 sources that merge in the tropical Indian Ocean (Fig. 5). One is related to the mid-latitude  
292 anticyclone over the northern Pacific Ocean and the other is related to the mid-latitude  
293 anticyclone over the northern Atlantic Ocean, which are associated with southward airflow  
294 across the Indo-Pacific Warm Pool and North Africa, respectively (Fig. 5). Therefore, the  
295 mid-latitude oceans in the Northern Hemisphere are the main source of water vapor supply  
296 for the dynamic enhancement of the horizontal moisture transport. This is in agreement  
297 with a recent study that showed mid-latitude atmospheric rivers were the dominant water  
298 vapor source for EASM precipitation changes during the MH relative to the PI period  
299 (Skinner et al. 2020). In contrast, there is a large reduction in the cross-equatorial airflow  
300 from the southern Indian Ocean, which is considered the main water vapor supply source  
301 for the mean state of EASM precipitation (Fig. 5). This means that the water vapor supply  
302 for EASM precipitation changes does not necessarily come from the strongest water vapor  
303 pathway for mean EASM precipitation.

304

### 305 **3.3.3 Reduced thermodynamic role due to cloud cooling**

306 The thermodynamic effect on precipitation is closely related to surface temperature  
307 changes. Therefore, quantifying the relative contribution of different processes to surface  
308 temperature changes with CFRAM (Cai and Lu 2009; Lu and Cai 2009) enables us to  
309 assess which processes affected surface temperature and, in turn, the reduced  
310 thermodynamic effect on precipitation. It would be expected that a thermodynamic  
311 increase (decrease) in precipitation is associated with surface warming (cooling). As such,  
312 the potential physical processes that cool Earth's surface are an underlying cause of the  
313 reduced thermodynamic role in the precipitation increase during the MH.

314 By decomposition of the “southern cooling and northern warming” pattern into nine  
315 processes (Fig. 1a versus Fig. 6), it was shown that the cloud cooling effect counteracts the  
316 main warming effect due to solar insolation, and thus led to this “southern cooling and  
317 northern warming” pattern over China (Fig. 6). The remaining five terms generally show  
318 either weak surface warming over mainland China (Fig. 6a, d, f, and g) in the absence of  
319 surface cooling required to sustain spatial heterogeneity (Fig.1a), or an opposite pattern  
320 due to surface dynamic processes affecting the total SAT changes (Fig. 6i). In addition,  
321 surface cooling due to ATH and CH<sub>4</sub> is so weak that their contribution to the overall SAT  
322 changes can be ignored (Fig. 6c and h). In summary, in addition to their dominant role in  
323 the southern cooling and northern warming over East Asia, cloud processes were also  
324 dominant in controlling the global surface cooling (not shown). One remaining question is  
325 how the surface cooling due to cloudiness affected the monsoon precipitation.

326 Based on the Clausius–Clapeyron relationship, the atmospheric water vapor content  
327 decreases with cooling and increases with warming. The damping effects of cloud on

328 EASM precipitation via regional surface cooling causes water vapor in the atmosphere to  
329 decline, and thus decreases the water supply available for precipitation. This is the primary  
330 reason for the weak thermodynamic effect during the MH. This result contrasts with the  
331 significant thermodynamic effect on EASM precipitation increase/decrease in other  
332 warm/cold climates (Sun et al. 2016, 2018, 2021).

333

#### 334 **4. Summary and conclusions**

335 We used proxy data and PMIP simulations to analyze orbital-scale climate variations in the  
336 EASM during the MH, when precession was quite different from the present day. Our  
337 results revealed distinct monsoonal dynamics at the orbital scale from those projected for  
338 future climate (Sun et al. 2018). Horizontal moisture advection controlled EASM  
339 precipitation changes during the MH in both the proxy records and models, and our  
340 findings reconcile the regional precipitation changes as determined by proxy records and  
341 models. Figure 7 summarizes our key findings, which are:

- 342 1. A quantitative data–model comparison revealed heterogeneity in the MH surface  
343 climate over the EASM domain. There was an overall increase in EASM precipitation  
344 in the proxy data and models, except for a few areas where there was a local decrease  
345 in precipitation, which was associated with a reduction in meridional thermal contrast  
346 (i.e., the southern cooling and northern warming pattern) over the EASM domain.
- 347 2. By decomposing the moisture budget, we developed a physical understanding of the  
348 spatial heterogeneity of EASM precipitation changes in the proxy data and models.  
349 Compared with vertical moisture advection, horizontal moisture advection had a larger  
350 role in determining the overall regional increase and local decrease in precipitation.

351 Dynamic enhancement of horizontal moisture advection can explain the overall  
352 increase in precipitation in the simulations and most of the wetter MH proxy records  
353 (106 of 126) over the EASM domain. The remaining proxy records of wetter East Asia  
354 conditions resulted from a weak thermodynamic contribution to increasing horizontal  
355 moisture advection. In contrast, localized decreases in precipitation from the proxy  
356 records and models are controlled by two different processes. Drier MH condition in  
357 21 proxy records reflect a decrease in the NL component of horizontal moisture  
358 advection, while a dynamic decrease in vertical moisture advection generated a drier  
359 eastern Tibetan Plateau in the simulations.

360 3. Stationary eddy activity is a mechanism that dynamically controls the regional  
361 precipitation. The dynamic enhancement of horizontal moisture advection that  
362 increased EASM precipitation was due mainly to the intensification of stationary eddy  
363 horizontal circulation over the EASM domain during the MH. In contrast, a dynamic  
364 decrease in the stationary eddy vertical motion resulted in a drier eastern Tibetan  
365 Plateau in the MH.

366 4. The cloud cooling effect was the dominant process responsible for surface cooling over  
367 the EASM domain, and is thus dominant in producing a southern cooling and northern  
368 warming pattern over China. Surface cooling due to cloud processes might have caused  
369 a reduction in the thermodynamic contribution to horizontal moisture advection and an  
370 increase in precipitation during the MH.

371 5. Mid-latitude oceans in the Northern Hemisphere were the water vapor supply source  
372 for the dynamic enhancement of horizontal moisture transport, whereas water vapor  
373 transport from the strongest pathway during the mean state of EASM precipitation was

374 reduced during the MH.

375

### 376 **Acknowledgements**

377

378 We thank the World Climate Research Program's Working Group on Coupled Modeling,

379 which is responsible for CMIP, and the climate modeling groups (Fig. 1) for producing and

380 making available their model outputs. All the simulations are publicly available on a

381 website ([https://www.ipcc-data.org/sim/gcm\\_monthly/AR5/Reference-Archive.html](https://www.ipcc-data.org/sim/gcm_monthly/AR5/Reference-Archive.html) and

382 <https://esgf-node.llnl.gov/projects/cmip6/>). Pollen-based reconstructions are open access

383 ([http://data.lasg.ac.cn/sunyong/pollen-based\\_reconstructions.pdf](http://data.lasg.ac.cn/sunyong/pollen-based_reconstructions.pdf)). We also thank Camille

384 Risi from the Laboratoire de Météorologie Dynamique, Paris, for insightful comments on

385 an earlier version of our manuscript. This research was jointly supported by the National

386 Key Research and Development Program of China (Grant 2018YFA0606003), National

387 Program on Key Basic Research Project of China (Grant 2017YFA0604601), Second

388 Tibetan Plateau Scientific Expedition and Research (STEP) program (Grant

389 2019QZKK0102), National Natural Science Foundation of China (NSFC; Grant

390 41661144009), GOTHAM international cooperative project, National Key Research and

391 Development Program of China (Grant 2018YFA0606003), and NSFC (Grants 41505076

392 and 41572165).

393

394 **References**

- 395 Braconnot P, Otto-Bliesner B, Harrison S, Joussaume S, Peterchmitt J-Y, Abe-Ouchi A,  
396 Crucifix M, Driesschaert E, Fichefet T, Hewitt CD, Kageyama M, Kitoh A, Laine A,  
397 Loutre M-F, Marti O, Merkel U, Ramstein G, Valdes P, Weber SL, Yu Y, Zhao Y  
398 (2007) Results of PMIP2 coupled simulations of the mid-Holocene and Last Glacial  
399 Maximum—part 1: experiments and large-scale features. *Clim Past* 3(2):261–277
- 400 Braconnot P, Harrison SP, Kageyama M, Bartlein PJ, Masson-Delmotte V, Abe-Ouchi A,  
401 Otto-Bliesner B, Zhao Y (2012) Evaluation of climate models using palaeoclimatic  
402 data. *Nat Clim Change* 2:417–424
- 403 Brierley C, Zhao A, Harrison S, Braconnot P, Williams C, Thornalley D, Shi X,  
404 Peterschmitt J-Y, Ohgaito R, Kaufman D, Kageyama M, Hargreaves J, Erb M, Emile-  
405 Geay J, D'Agostino R, Chandan D, Carré M, Bartlein P, Zheng W, Zhang Z, Zhang  
406 Q, Yang H, Volodin E, Tomas R, Routson C, Peltier W, Otto-Bliesner B, Morozova  
407 P, McKay N, Lohmann G, Legrande A, Guo C, Cao J, Brady E, Annan J, Abe-Ouchi  
408 A(2020) Large-scale features and evaluation of the PMIP4-  
409 CMIP6 *midHolocene* simulations. *Clim. Past Discuss*, [https://doi.org/10.5194/cp-](https://doi.org/10.5194/cp-2019-168)  
410 2019-168
- 411 Cai M, Lu JH (2009) A new framework for isolating individual feedback processes in  
412 coupled general circulation climate models. Part II: method demonstrations and  
413 comparisons. *Clim Dyn* 32:887–900
- 414 Chou C, Lan CW (2012) Changes in the annual range of precipitation under global  
415 warming. *J Clim* 25(1):222–235. <https://doi.org/10.1175/JCLI-D-11-00097.1>
- 416 COHMAP Members (1988) Climatic changes of the last 18,000 years: observations and  
417 model simulations. *Science* 241:1043–1052

418 D'Agostino R, Brown J R, Moise A, Nguyen H, Jungclaus J (2020) Contrasting Southern  
419 Hemisphere Monsoon Response: MidHolocene Orbital Forcing versus Future  
420 Greenhouse Gas–Induced Global Warming. *J Clim* 33(22), 9595-9613.

421 D'Agostino R, Bader J, Bordoni S, Ferreira D, Jungclaus J (2019) Northern Hemisphere  
422 monsoon response to mid-Holocene orbital forcing and greenhouse gas-induced  
423 global warming. *Geophys Res Lett* 46: 1591– 1601

424 Ding Y, Chan J (2005) The East Asian summer monsoon: an overview. *Meteorol Atmos*  
425 *Phys* 89:117–142

426 Hopcroft P, Valdes P (2019) On the role of dust-climate feedbacks during the mid-  
427 Holocene. *Geophys Res Lett* 46: 1612– 1621

428 Jiang D, Tian Z, Lang X (2015) Mid-Holocene global monsoon area and precipitation from  
429 PMIP simulations. *Clim Dyn* 44:2493–2512

430 Jiang W, Leroy SAG, Yang S, Zhang E, Wang L, Yang X, Rioual P (2019) Synchronous  
431 strengthening of the Indian and East Asian monsoons in response to global warming  
432 since the last deglaciation. *Geophys Res Lett* 46:3944–3952

433 Joussaume S, Taylor K, Braconnot P, Mitchell J, Kutzbach J, Harrison S, Prentice I,  
434 Broccoli A, Abe-Ouchi A, Bartlein P, Bonfils C, Dong B, Guiot J, Herterich K, Hewitt  
435 C, Jolly D, Kim J, Kislov A, Kitoh A, Loutre M, Masson V, McAvaney B, McFarlane  
436 N, de Noblet N, Peltier W, Peterschmitt J-Y, Pollard D, Rind D, Royer J, Schlesinger  
437 M, Syktus J, Thompson S, Valdes P, Vettoretti G, Webb R, Wyputta U (1999)  
438 Monsoon changes for 6000 years ago: results of 18 simulations from the  
439 Palaeoclimate Modelling Intercomparison Project (PMIP). *Geophys Res Lett* 26:859–  
440 862

441 Lin Y, Ramstein G, Wu H, Rani R, Braconnot P, Kageyama M, Li Q, Luo Y, Zhang R,  
442 Guo Z (2019) Mid-Holocene climate change over China: model–data discrepancy.  
443 *Clim Past* 15(4): 1223–1249

444 Liu Z, Harrison S, Kutzbach J, Otto–Bliesner B (2004) Global monsoons in the mid–  
445 Holocene and oceanic feedback. *Clim Dyn* 22: 157–182

446 Liu Z, Zhu J, Rosenthal Y, Zhang X, Otto-Gliesner BL, Timmermann A, Smith RS,  
447 Lohmann G, Zheng W, Timm OE (2014) The Holocene temperature conundrum. *Proc*  
448 *Natl Acad Sci* 11:3501–3505

449 Lu J, Cai M (2009) A new framework for isolating individual feedback processes in  
450 coupled general circulation climate models. Part I: Formulation. *Clim Dyn* 32: 873–  
451 885

452 Otto-Bliesner BL et al (2017) The PMIP4 contribution to CMIP6—Part 2: two interglacials,  
453 scientific objective and experimental design for Holocene and Last Interglacial  
454 simulations. *Geosci Model Dev* 10:3979–4003

455 Patricola C, Cook K (2007) Dynamics of the West African Monsoon under Mid-Holocene  
456 Precessional Forcing: Regional Climate Model Simulations. *J Clim* 20:694–716

457 Pausata F, Messori G, Zhang Q (2016) Impacts of dust reduction on the northward  
458 expansion of the African monsoon during the Green Sahara period. *Earth Planet Sci*  
459 *Lett* 434:298–307

460 Piao J, Chen W, Wang L, Pausata F, Zhang Q (2020) Northward extension of the East  
461 Asian summer monsoon during the mid-Holocene. *Glob Planet Change* 184:  
462 <https://doi.org/10.1016/j.gloplacha.2019.103046>

463 Shin S-I, Sardeshmukh PD, Webb RS, Oglesby RJ, Barsugli JJ (2006) Understanding the  
464 Mid-Holocene Climate. *J Clim* 19:2801–2817. doi:10.1175/JCLI3733.1

465 Skinner C, Lora J, Payne A, Poulsen C (2020) Atmospheric river changes shaped mid-  
466 latitude hydroclimate since the mid-Holocene. *Earth Planet Sci Lett* 541:  
467 <https://doi.org/10.1016/j.epsl.2020.116293>

468 Steig E (1999) Mid-Holocene Climate Change. *Science*, 286:148–149.

469 Sun W, Wang B, Zhang Q, Pausata F, Chen D, Lu G, Yan M, Ning L, Liu J (2019) Northern  
470 Hemisphere land monsoon precipitation increased by the Green Sahara during middle  
471 Holocene. *Geophys Res Lett* 46: 9870–9879

472 Sun Y, Zhou T, Ramstein G, Contoux C, Zhang Z (2016) Drivers and mechanisms for  
473 enhanced summer monsoon precipitation over East Asia during the mid-Pliocene in  
474 the IPSL-CM5A. *Clim Dyn* 46:1437–1457

475 Sun Y, Ramstein G, Li L, Contoux C, Tan N, Zhou T (2018) Quantifying East Asian  
476 summer monsoon dynamics in the ECP4.5 scenario with reference to the mid-  
477 Piacenzian warm period. *Geophys Res Lett* 45: 12523–12533

478 Sun Y, Wu H, Kageyama M, Ramstein G, Li L, Tan N, Lin Y, Liu B, Zheng W, Zhang W,  
479 Zou L, Zhou T (2021) The contrasting effects of thermodynamic and dynamic  
480 processes on East Asian summer monsoon precipitation during the Last Glacial  
481 Maximum: a data-model comparison. *Clim Dyn* 56: 1303–1316

482 Wang B, Liu J, Kim H, Webster P, Yim S (2012) Recent change of the global monsoon  
483 precipitation (1979–2008). *Clim Dyn* 39:1123–1135

484 Wang N, Jiang D, Lang X (2020) Mechanisms for Spatially Inhomogeneous Changes in  
485 East Asian Summer Monsoon Precipitation during the Mid-Holocene. *J Clim* 33:  
486 2945–2965

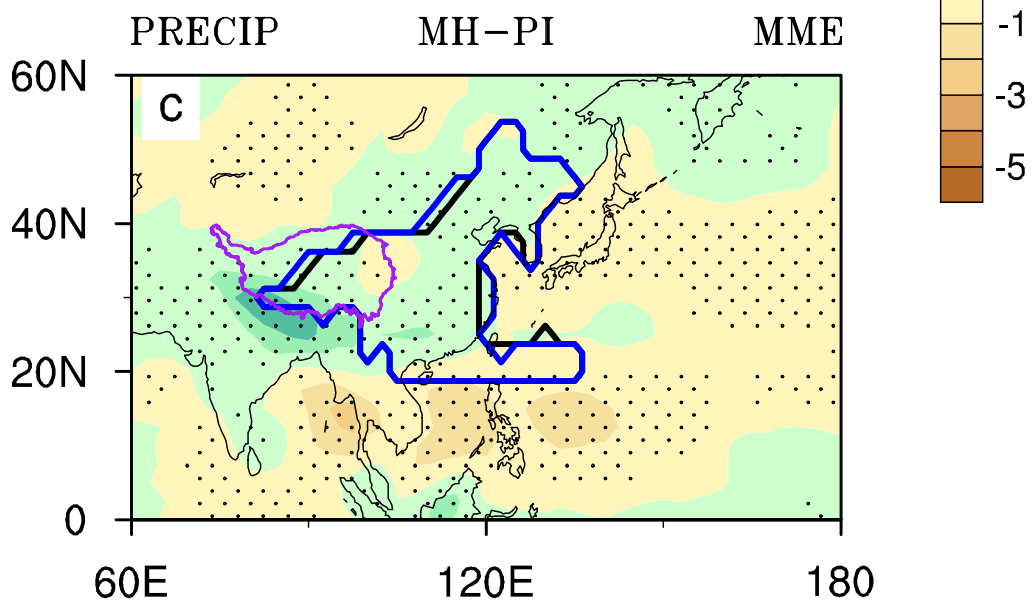
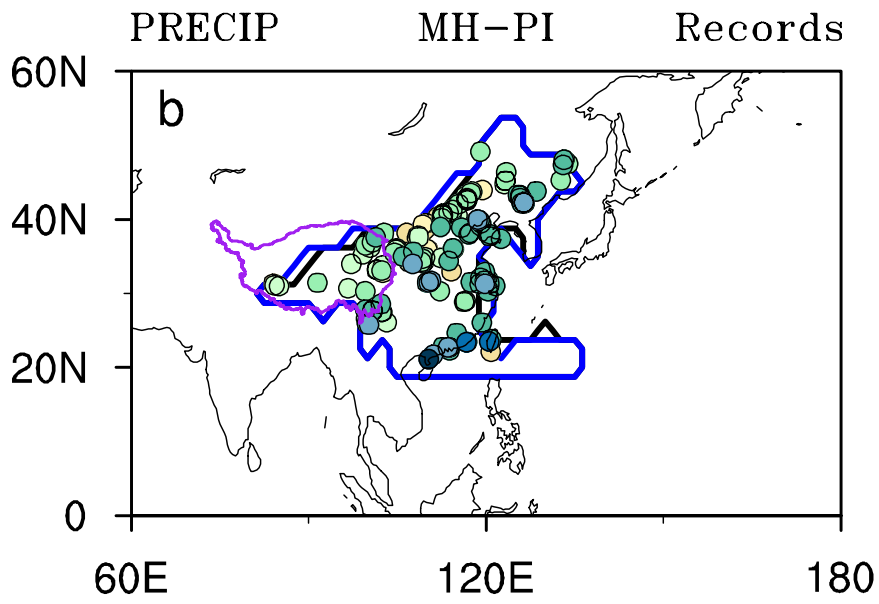
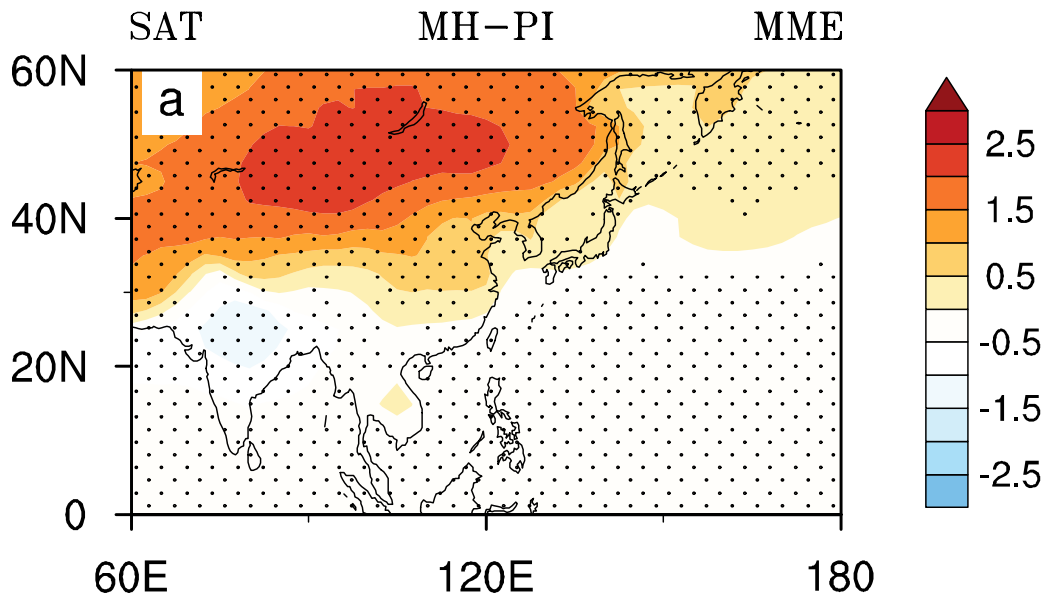
487 Zhao Y, Braconnot P, Marti O, Harrison S, Hewitt C, Kitoh A, Liu Z, Mikolajewicz U,  
488 Otto-Bliesner B, Weber S (2005) A multimodel analysis of role of ocean feedback on  
489 the African and Indian monsoon during Mid-Holocene. *Clim Dyn* 25:777–800

490 Zhao Y, Harrison SP (2012) Mid-Holocene monsoons: a multi-model analysis of the inter-  
491 hemispheric differences in the response to the orbital forcing and ocean feedbacks.  
492 *Clim Dyn* 39:1457–1487

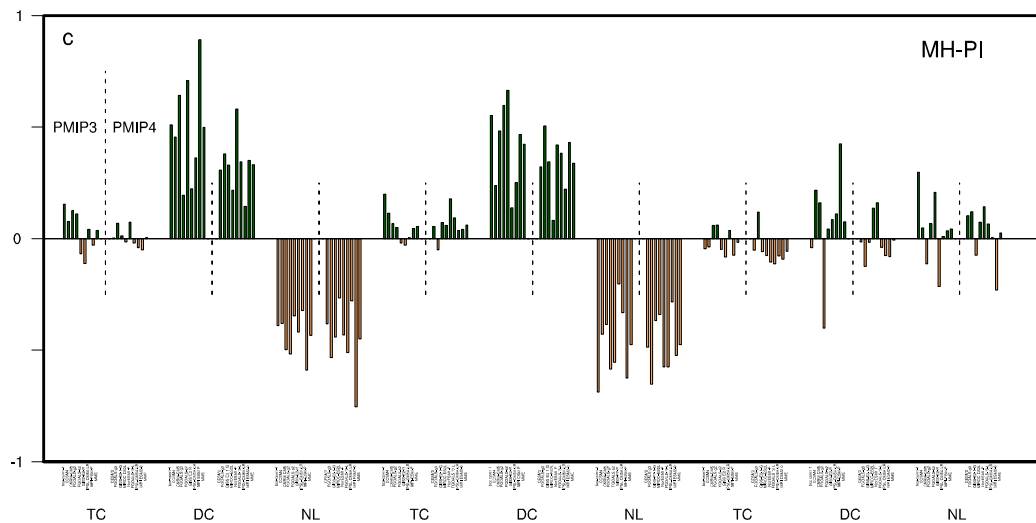
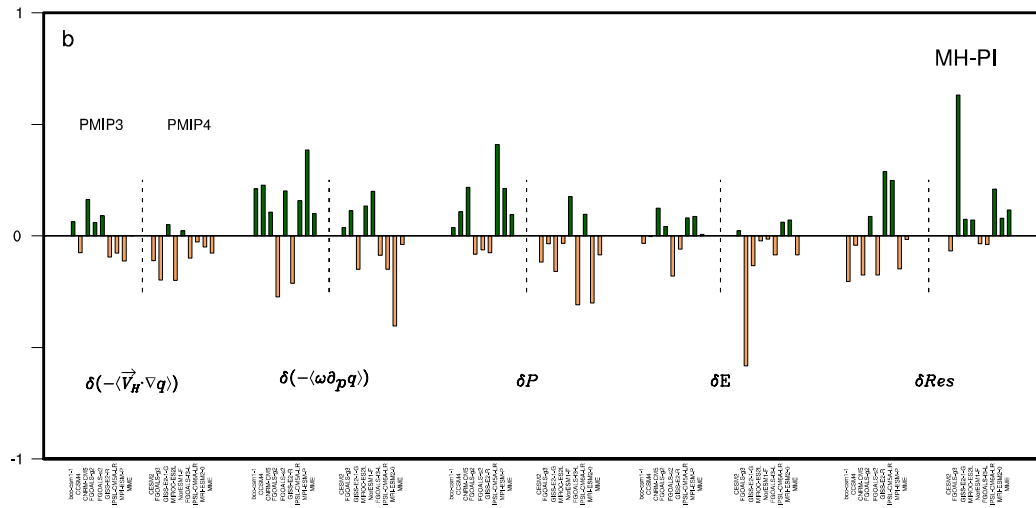
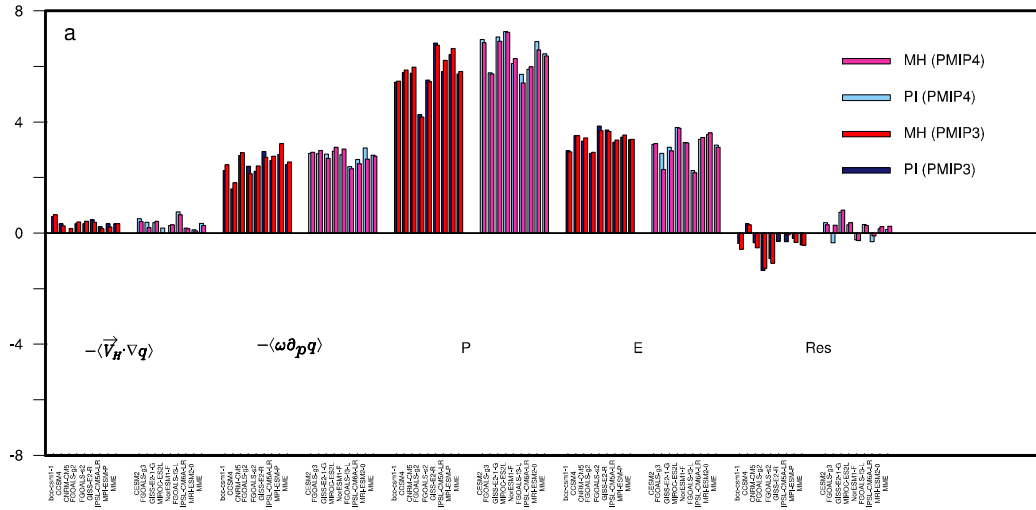
493

494 **Figures**

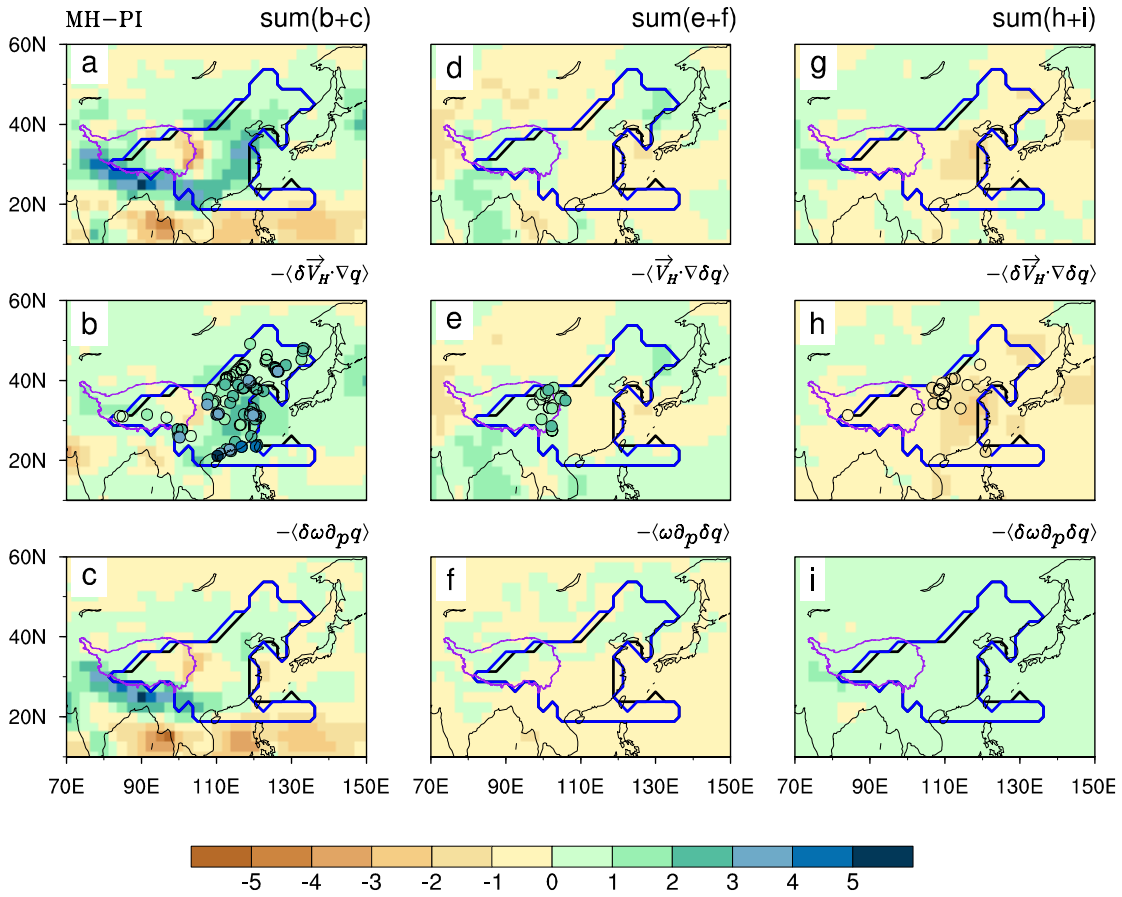
495



497 **Figure 1.** Spatial patterns of mean June–July–August (JJA) surface air temperature (SAT  
498 in °C; top panel) and precipitation (PRECIP in mm/day) changes during the mid-Holocene  
499 (MH) compared with pre-industrial (PI) levels derived from pollen-based reconstructions  
500 (middle panel) and the multi-model ensemble (MME) of the three PMIP phases (bottom  
501 panel). Areas with a significance above the 1% level are stippled. Black and blue lines on  
502 the right panels are the East Asian Summer Monsoon (EASM) domain in the PI period and  
503 MH, respectively. The purple line outlines the Tibetan Plateau (data source:  
504 <http://www.geodoi.ac.cn/weben/doi.aspx?Id=135>). Colored circle symbols in (b) use the  
505 same color scale as the MME and represent pollen-based reconstructions (147 sites within  
506 the EASM domain) for the MH.  
507

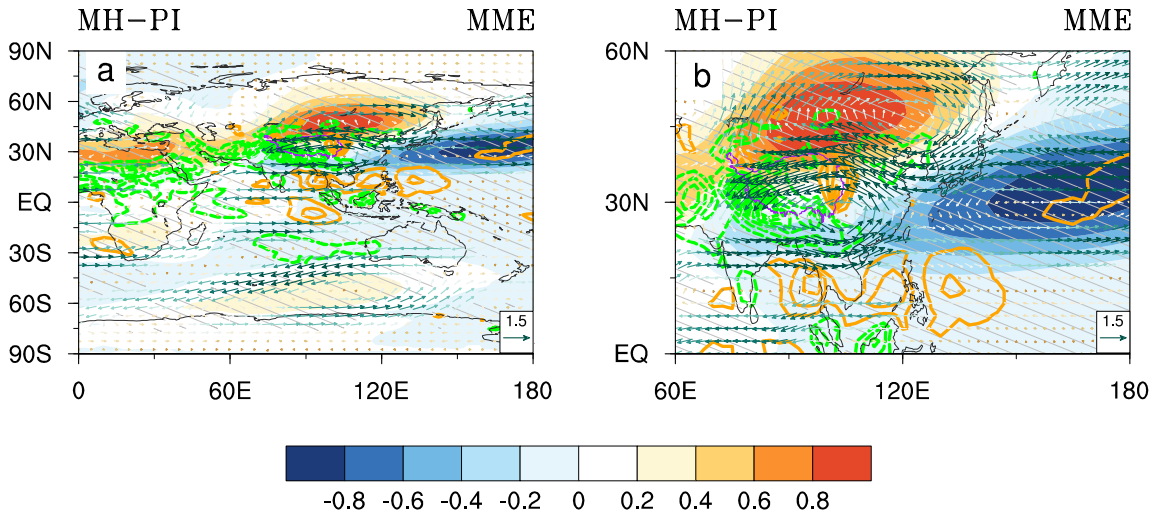


509 **Figure 2.** Results from the moisture budget equation used to resolve water vapor processes  
510 related to mean precipitation for the **(a)** MH and PI periods and **(b)** differences between  
511 the MH and PI periods. The two difference terms in **(b)** were decomposed into three  
512 processes in **(c)** to quantify the relative contribution from changes due to specific humidity  
513 with fixed atmospheric circulation (thermodynamic component; TC), atmospheric  
514 circulation with constant specific humidity (dynamic component; DC), and simultaneous  
515 changes in both specific humidity and atmospheric circulation (i.e., non-linear term; NL).  
516



517

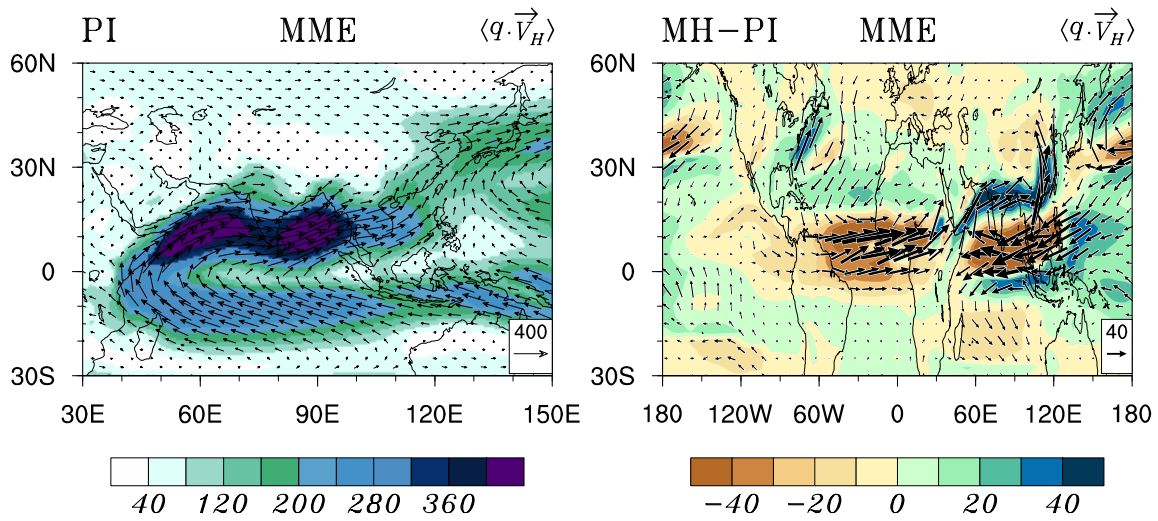
518 **Figure 3.** Pollen-based precipitation records and spatial patterns of the three decomposed  
 519 processes for the two moisture advection patterns shown in Fig. 2c. The physical processes  
 520 (from left to right in each subfigure) are DC, TC, and NL. (c, f, i) Vertical moisture  
 521 advection. (b, e, h) Horizontal moisture advection. (a, d, g) Sum of the two moisture  
 522 advections. The 126 green circle symbols (106 in (b) and 20 in (e)) indicate wetter East  
 523 Asia conditions, and the 21 yellow circle symbols in (h) indicate drier East Asia conditions.



524

525 **Figure 4. (a)** Differences between the three vertically integrated variables throughout the  
 526 troposphere between the MH and PI periods, which are termed the stationary eddy  
 527 horizontal circulation (colored vectors; color bar not shown), stationary eddy vertical  
 528 velocity (contours), and air temperature (shading with color bar). (b) Enlarged view of (a)  
 529 over the EASM domain. Gray dashed lines are the stationary eddy air temperature above  
 530 the 1% level. Positive vertical velocity values indicate descending motion (orange solid  
 531 contours), and negative values represent ascending motion (green dashed contours).

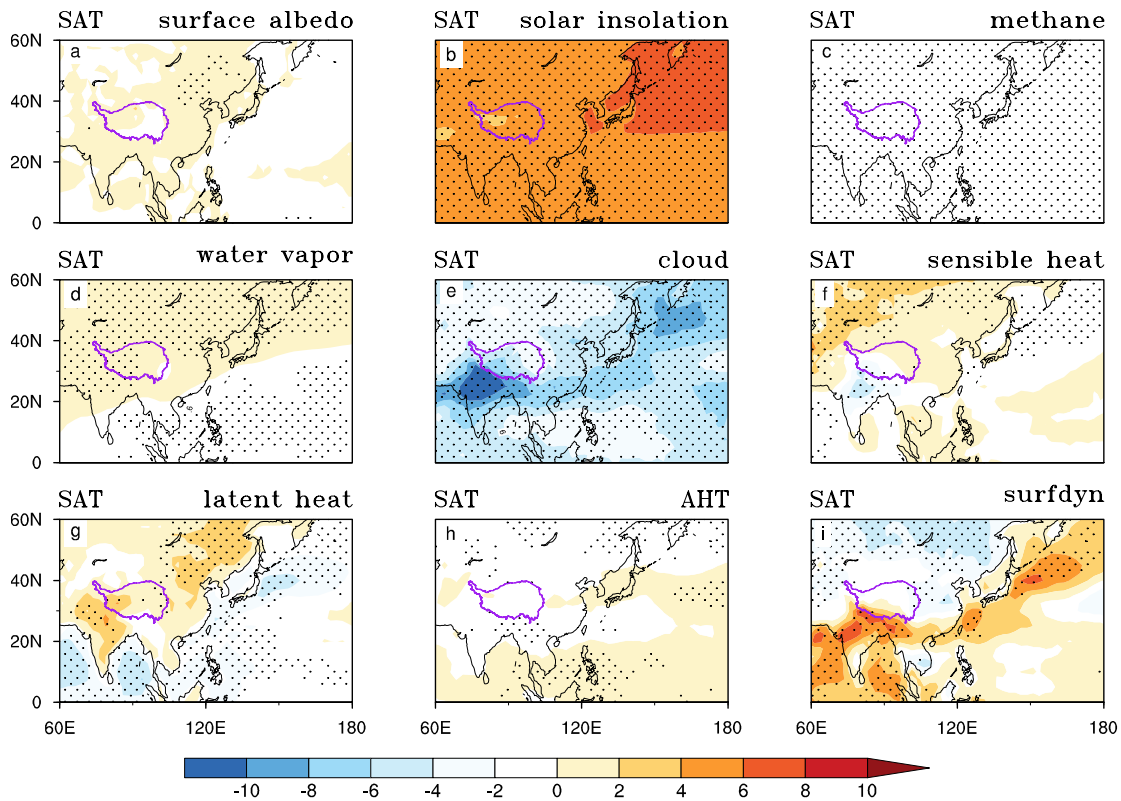
532



533

534 **Figure 5.** Large-scale moisture transport as determined by the vertically integrated  
 535 moisture flux ( $\langle q \cdot \vec{V} \rangle$  in  $\text{kg} \cdot \text{m}^{-1} \cdot \text{s}^{-1}$ ) across the whole troposphere in the boreal summer  
 536 (JJA). (a) Climatology of the PI period. (b) Differences between the MH and PI periods.

537

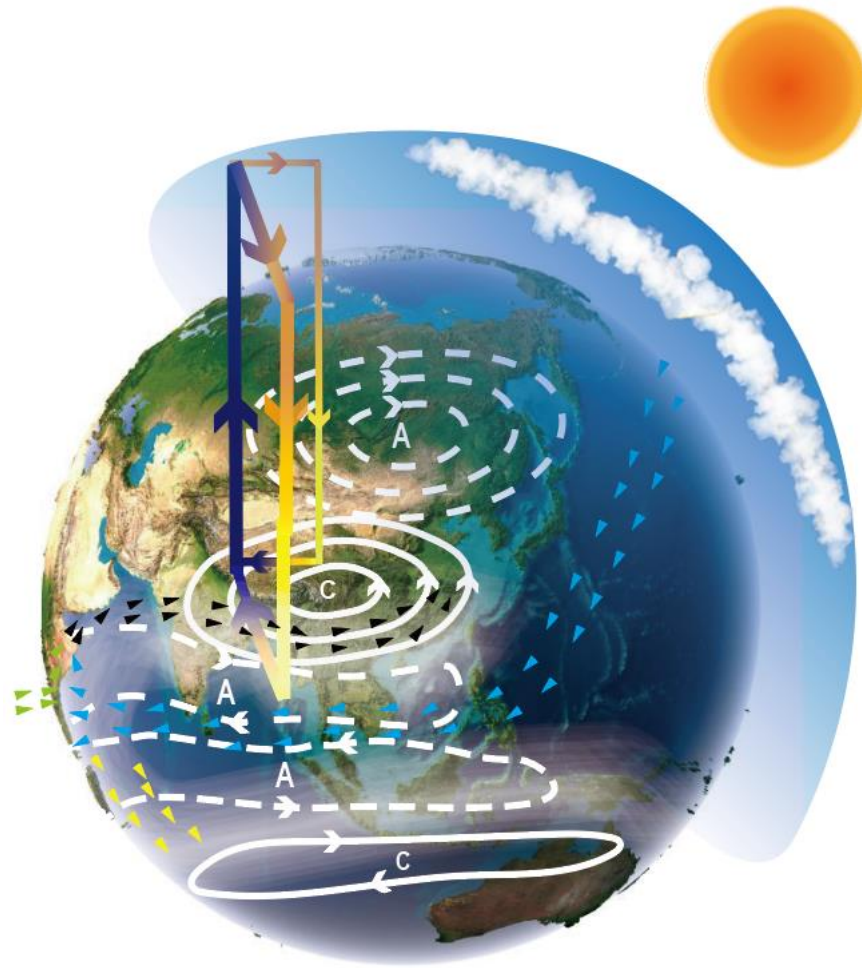


538

539 **Figure 6.** CFRAM-based decompositions of SAT changes (in °C) in the MH relative to the  
 540 PI period (as shown in Fig. 1a), as represented by nine processes. AHT and surfdyn in (h–  
 541 i) are the atmospheric heat transport and surface dynamic processes, respectively. This  
 542 decomposition was derived from an MME of PMIP3. Stippled areas show that seven of the  
 543 eight models have the same sign.

544

545



546  
 547 **Figure 7.** Schematic illustration of the physics underlying monsoon precipitation responses  
 548 to orbital forcing under MH climate conditions, including the dynamic strengthening and  
 549 thermodynamic damping roles in an overall increase in EASM precipitation and a dynamic  
 550 decrease in precipitation during the MH. Regional dynamic enhancement is part of the  
 551 global-scale stationary eddy wave trains that consist of stationary eddy cyclones (C) and  
 552 anticyclones (A) in the Northern and Southern hemispheres. The thermodynamic  
 553 contribution to the increase in precipitation is reduced by the cloud cooling effect. Vapor  
 554 sources of intensified moisture transport into the EASM domain are due to intensified  
 555 stationary eddy circulation (black arrows) from the mid-latitude northern Pacific Ocean

556 (blue arrows) and northern Atlantic Ocean (green arrows). In contrast, cross-equatorial  
557 airflow originates in the southern Indian Ocean which is considered the strongest water  
558 vapor supply source for the mean state of EASM precipitation is decreased during the MH  
559 (orange arrows).

# Figures

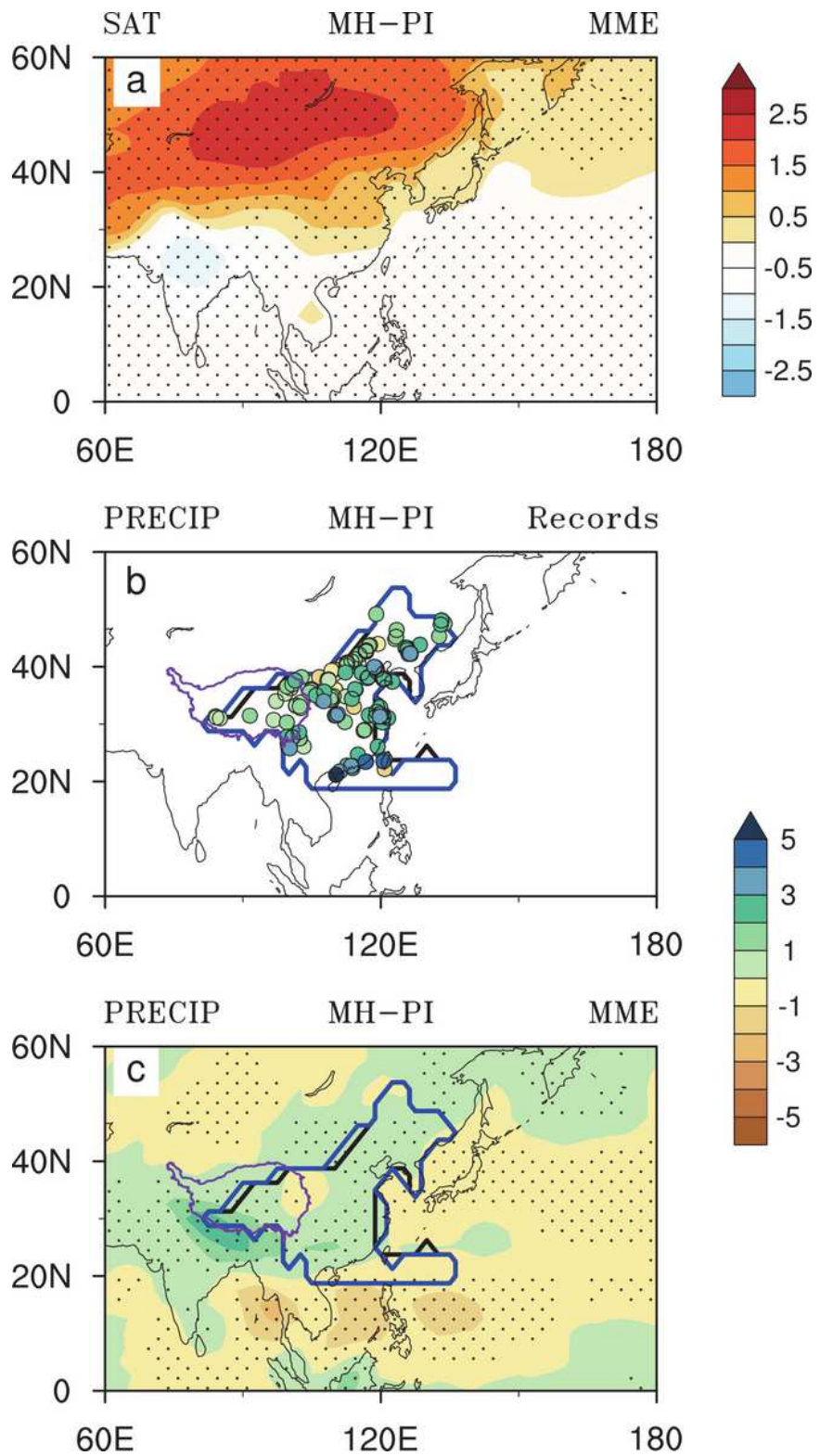


**Figure 1**

Spatial patterns of mean June–July–August (JJA) surface air temperature (SAT in °C; top panel) and precipitation (PRECIP in mm/day) changes during the mid-Holocene (MH) compared with pre-industrial (PI) levels derived from pollen-based reconstructions (middle panel) and the multi-model ensemble

(MME) of the three PMIP phases (bottom panel). Areas with a significance above the 1% level are stippled. Black and blue lines on the right panels are the East Asian Summer Monsoon (EASM) domain in the PI period and MH, respectively. The purple line outlines the Tibetan Plateau (data source: <http://www.geodoi.ac.cn/weben/doi.aspx?Id=135>). Colored circle symbols in (b) use the same color scale as the MME and represent pollen-based reconstructions (147 sites within the EASM domain) for the MH. Note: The designations employed and the presentation of the material on this map do not imply the expression of any opinion whatsoever on the part of Research Square concerning the legal status of any country, territory, city or area or of its authorities, or concerning the delimitation of its frontiers or boundaries. This map has been provided by the authors.

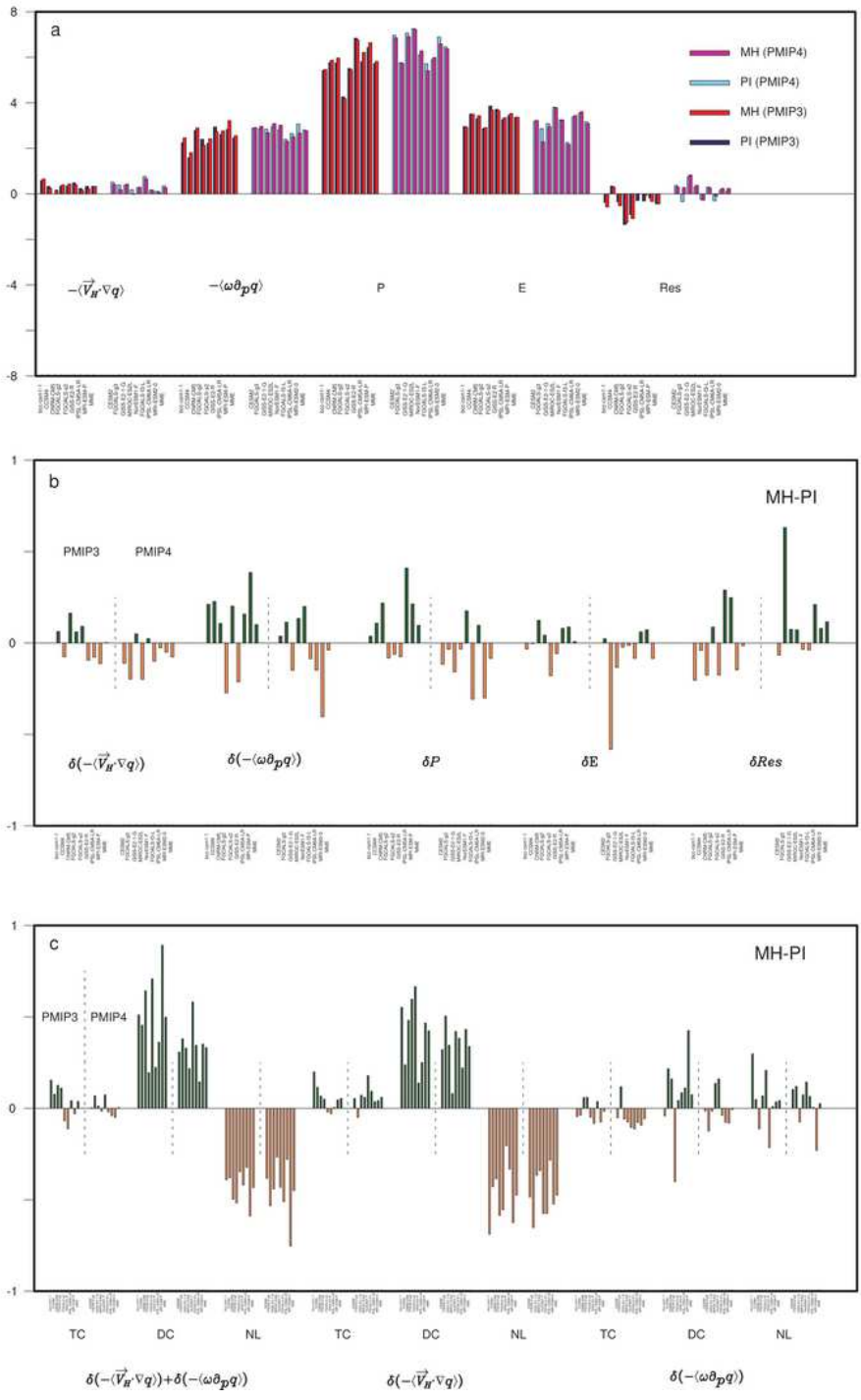


**Figure 2**

Results from the moisture budget equation used to resolve water vapor processes related to mean precipitation for the (a) MH and PI periods and (b) differences between the MH and PI periods. The two difference terms in (b) were decomposed into three processes in (c) to quantify the relative contribution from changes due to specific humidity with fixed atmospheric circulation (thermodynamic component;

TC), atmospheric circulation with constant specific humidity (dynamic component; DC), and simultaneous changes in both specific humidity and atmospheric circulation (i.e., non-linear term; NL).

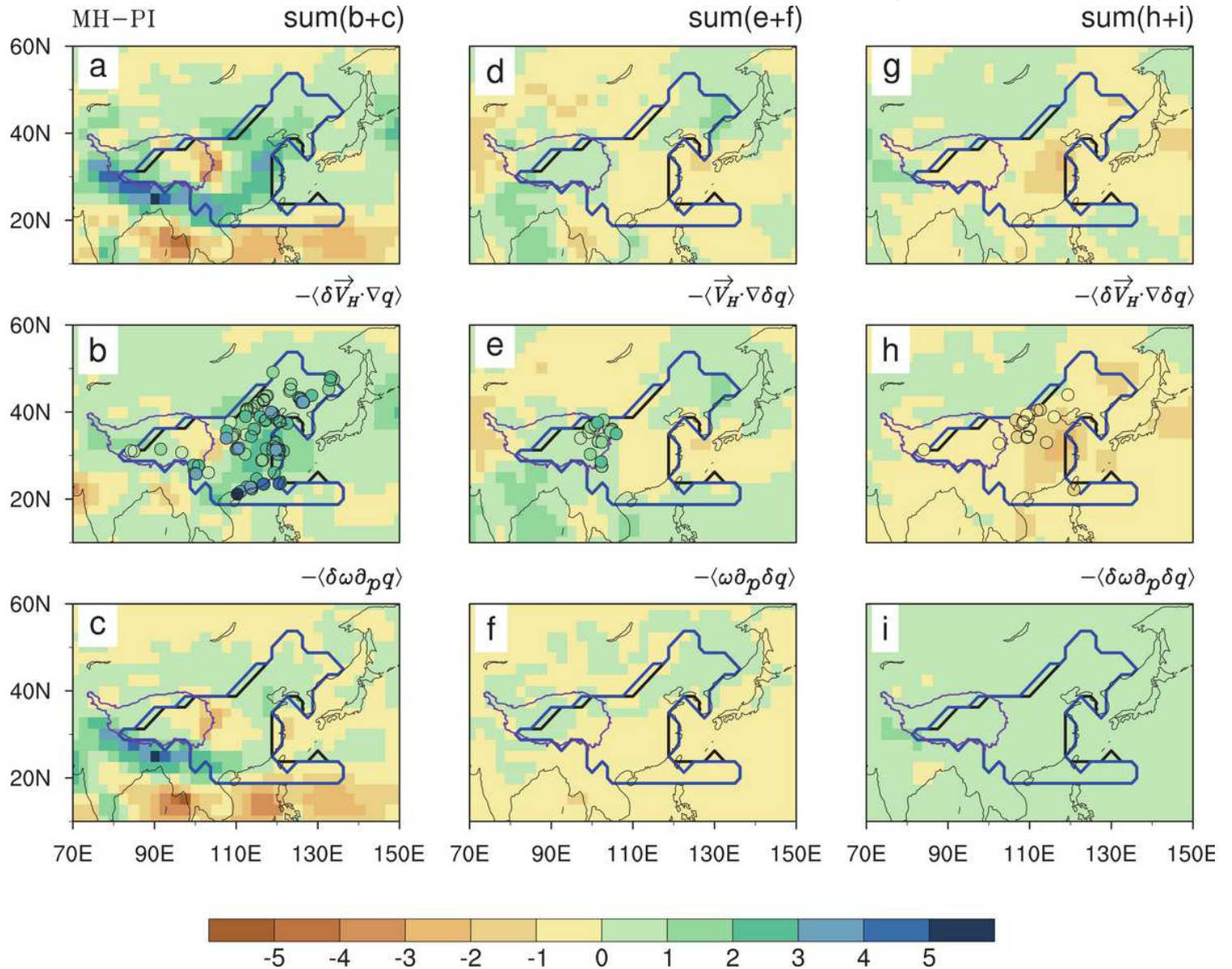


**Figure 3**

Pollen-based precipitation records and spatial patterns of the three decomposed processes for the two moisture advection patterns shown in Fig. 2c. The physical processes (from left to right in each subfigure) are DC, TC, and NL. (c, f, i) Vertical moisture advection. (b, e, h) Horizontal moisture advection. (a, d, g) Sum of the two moisture advections. The 126 green circle symbols (106 in (b) and 20 in (e)) indicate wetter East Asia conditions, and the 21 yellow circle symbols in (h) indicate drier East Asia conditions. Note: The designations employed and the presentation of the material on this map do not imply the expression of any opinion whatsoever on the part of Research Square concerning the legal status of any country, territory, city or area or of its authorities, or concerning the delimitation of its frontiers or boundaries. This map has been provided by the authors.

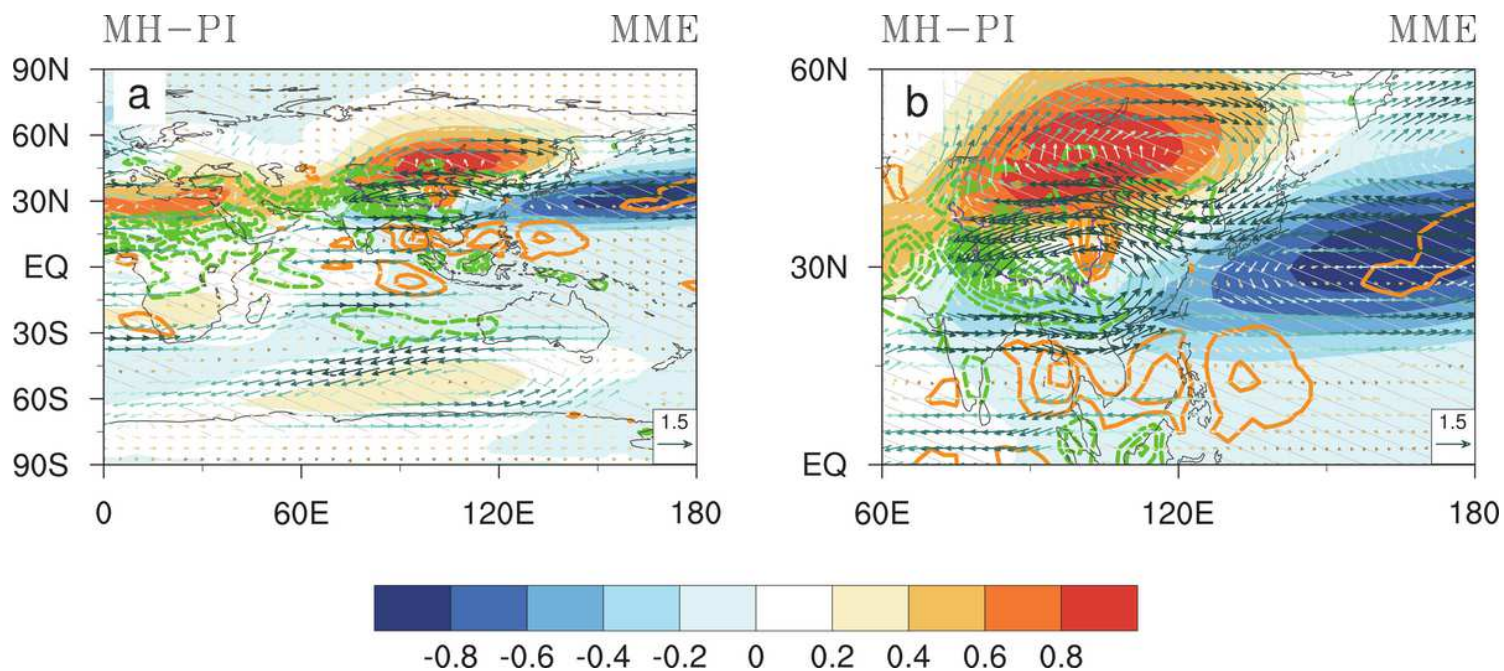


**Figure 4**

(a) Differences between the three vertically integrated variables throughout the troposphere between the MH and PI periods, which are termed the stationary eddy horizontal circulation (colored vectors; color bar not shown), stationary eddy vertical velocity (contours), and air temperature (shading with color bar). (b) Enlarged view of (a) over the EASM domain. Gray dashed lines are the stationary eddy air temperature above the 1% level. Positive vertical velocity values indicate descending motion (orange solid contours), and negative values represent ascending motion (green dashed contours). Note: The designations employed and the presentation of the material on this map do not imply the expression of any opinion whatsoever on the part of Research Square concerning the legal status of any country, territory, city or area or of its authorities, or concerning the delimitation of its frontiers or boundaries. This map has been provided by the authors.

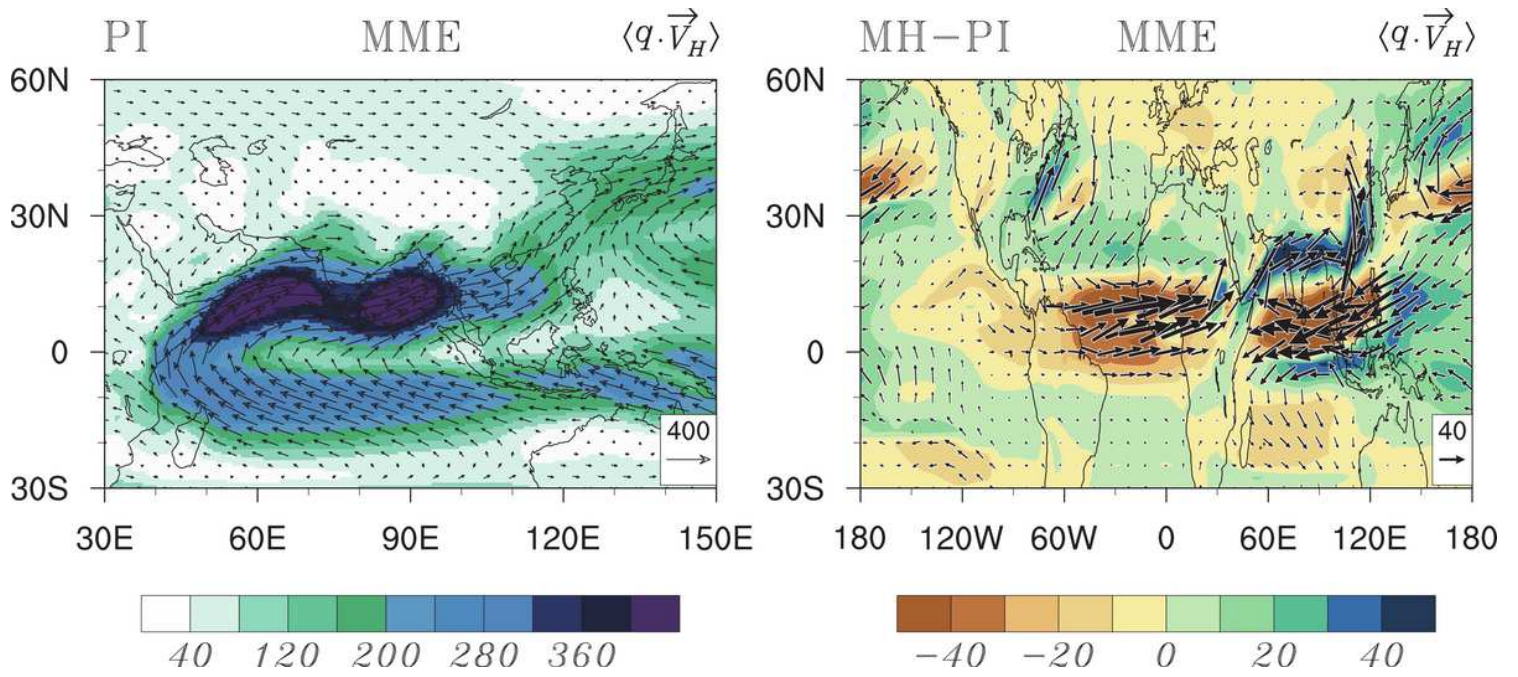


**Figure 5**

Please see the Manuscript PDF file for the complete figure caption. Note: The designations employed and the presentation of the material on this map do not imply the expression of any opinion whatsoever on the part of Research Square concerning the legal status of any country, territory, city or area or of its authorities, or concerning the delimitation of its frontiers or boundaries. This map has been provided by the authors.

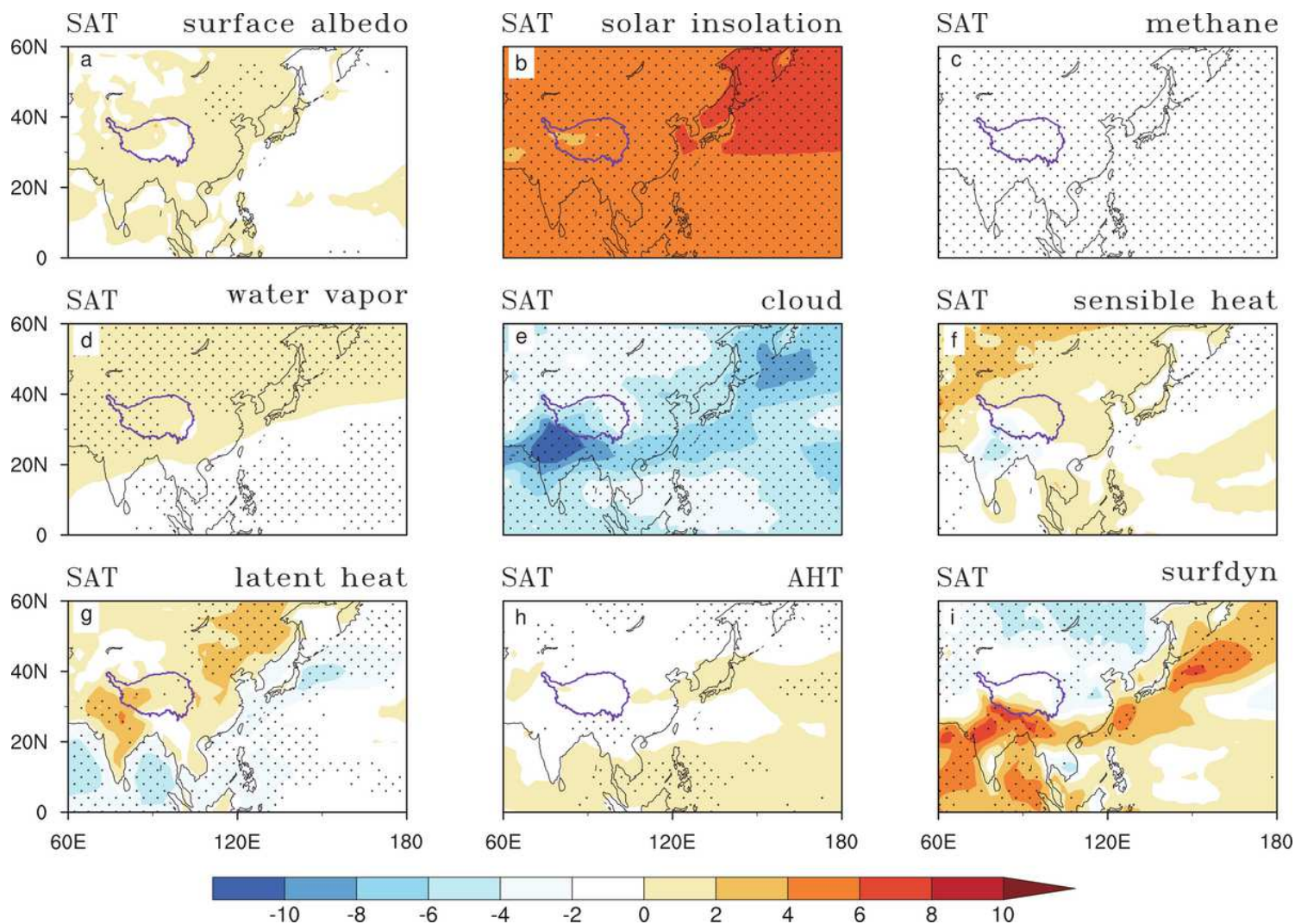


**Figure 6**

CFRAM-based decompositions of SAT changes (in °C) in the MH relative to the PI period (as shown in Fig. 1a), as represented by nine processes. AHT and surfdyn in (h–i) are the atmospheric heat transport and surface dynamic processes, respectively. This decomposition was derived from an MME of PMIP3. Stippled areas show that seven of the eight models have the same sign. Note: The designations employed and the presentation of the material on this map do not imply the expression of any opinion whatsoever on the part of Research Square concerning the legal status of any country, territory, city or area or of its authorities, or concerning the delimitation of its frontiers or boundaries. This map has been provided by the authors.

## Supplementary Files

This is a list of supplementary files associated with this preprint. Click to download.

- [resubSupp.docx](#)